

Pre-Virialized Assembly at Cosmic Dawn: The Dynamics and Extreme Ionization of Compact Group CGG-z7 at $z \sim 7.04$

XIAOYANG WEI ¹, ZHENG CAI ¹, FUJIANG YU ¹, MINGYU LI ¹ AND YUNJING WU ²

¹*Department of Astronomy, Tsinghua University, Beijing 100084, China*

²*Kavli Institute for the Physics and Mathematics of the Universe (WPI), The University of Tokyo Institutes for Advanced Study, The University of Tokyo, Kashiwa, Chiba 277-8583, Japan*

ABSTRACT

We report the discovery of CGG-z7, the most compact galaxy group at $z \gtrsim 7$ identified to the north of the GOODS-North field, observed by the JWST POPPIES program. The system consists of at least six members within a projected size of 7.8×5.7 kpc², four of which are spectroscopically confirmed via [O III] and H β emission. The group exhibits a low line-of-sight velocity dispersion (≈ 93.7 km s⁻¹) relative to its substantial stellar mass ($M_* \approx 10^{9.8} M_\odot$), yielding a stellar-to-dynamical mass ratio of $M_*/M_{\text{vir}} \approx 0.15$. This ratio, exceeding typical values for virialized halos by a factor of 3, indicates that the system is highly likely not in dynamical equilibrium. Instead, we interpret CGG-z7 as a pre-virialized structure, likely a major merger caught near apocenter—capturing the rapid, chaotic formation of a massive “Red Nugget”. Spectroscopic analysis reveals extreme ionization conditions and low metallicity across the group. In particular, the central galaxy reaches an extraordinarily high [O III]/H β ratio of ~ 18 , which is likely indicative of an obscured AGN. CGG-z7 thus serves as a unique laboratory for the physics of pre-virialized galaxy assembly, bridging the gap between turbulent high- z assembly and the quiescent galaxies seen at cosmic noon.

1. INTRODUCTION

Compact galaxy groups are predicted to be a crucial transition stage—the immediate precursors to massive, coalesced systems (R. S. Somerville & R. Davé 2015; S. Jin et al. 2023; M. Brinch et al. 2025; A. Saxena et al. 2025). Critically, such dense structures within larger overdense regions (protoclusters) are predicted to account for a dominant fraction of the cosmic star formation activity at high redshift (e.g., Y.-K. Chiang et al. 2013, 2017; P. Staab et al. 2024), making them key laboratories for early galaxy assembly. Within such environments, galaxies experience frequent gravitational interactions and mergers, driving their rapid dynamical evolution (e.g., P. Hickson 1997; Y.-K. Chiang et al. 2017; S. Liu et al. 2025; C. Witten et al. 2025; Y. Fudamoto et al. 2025; M. Li et al. 2026).

Dense, pre-virialized structures represent a highly accelerated “fast-track” evolutionary pathway. While not all high-redshift overdensities are deterministically bound for immediate quiescence, the extreme kinematics within compact groups frequently trigger merger-driven compaction (A. Dekel & A. Burkert 2014; S. Tacchella et al. 2016). During this process, tidal torques efficiently

strip angular momentum, driving massive inflows of cold gas into galactic centers. This dissipative contraction forms ultra-dense, star-forming cores (A. Dekel & A. Burkert 2014; S. Lapiner et al. 2023).

Building on this compaction phase, frequent mergers and tidal forces continue to shape the gas distribution: while inflows funnel gas toward the center, outflows and stripping simultaneously remove gas from the galaxy outskirts, potentially triggering and fueling active galactic nuclei (AGN), while simultaneously accelerating gas consumption or ejection (e.g., P. F. Hopkins & E. Quataert 2011; J. M. Comerford & J. E. Greene 2014; D. Puskás et al. 2025; E. A. Shah et al. 2025; M. K. Shea et al. 2026). These processes make compact groups plausible progenitors of the dense, quiescent galaxies observed at later cosmic epochs (e.g., M. Ando et al. 2022; S. Jin et al. 2024; T. Kakimoto et al. 2024). In this picture, the fast-track compaction followed by AGN-driven gas depletion naturally bridges rapid assembly with subsequent quenching.

Despite the theoretical necessity of this fast-track pathway, state-of-the-art cosmological simulations continue to underpredict the abundance of massive quiescent galaxies at $z > 4$ by an order of magnitude (e.g., G. Girelli et al. 2019; A. C. Carnall et al. 2023; A. de Graaff et al. 2025). This tension persists largely because direct observational constraints on the pre-virialized merg-

ing and saturation phases during the epoch of reionization remain elusive. While several high-redshift compact groups have been identified (e.g., T. Díaz-Santos et al. 2018; N. B. Sillassen et al. 2022; S. Jin et al. 2023, 2024; L. Zhou et al. 2024; N. B. Sillassen et al. 2024; A. Saxena et al. 2025; M. Brinch et al. 2025; Y. Fudamoto et al. 2025), capturing a system precisely at the tipping point of dynamic instability and extreme ionization at $z > 7$ has remained out of reach. With its unique combination of sensitivity and spatial resolution, JWST finally enables us to identify such a transforming progenitor.

In this paper, we report the discovery of CGG-z7, a profoundly compact, dynamically young galaxy group at $z \sim 7.04$ revealed by JWST/NIRCam. By presenting extreme ionization conditions and non-virialized kinematics, CGG-z7 offers unprecedented direct evidence of saturation-phase assembly prior to coalescence and quenching. The structure of the paper is as follows. In Section 2, we describe the observations and data reduction. Section 3 details our analysis of the group’s morphology, kinematics, stellar populations, and emission-line properties. Finally, in Section 4, we provide a summary of our findings and discuss their implications. We adopt $H_0 = 73 \text{ km s}^{-1} \text{ Mpc}^{-1}$, $\Omega_m = 0.27$ and $\Omega_\Lambda = 0.73$ in our analysis. We use line wavelengths 4960.293\AA for $[\text{O III}]\lambda 4959$, 5008.239\AA for $[\text{O III}]\lambda 5007$ and 4862.670\AA for $\text{H}\beta$ based on the CHIANTI Database (K. P. Dere et al. 1997; G. Del Zanna et al. 2021)³.

2. DATA REDUCTION

The data in this paper come from the POPPIES program (J. Kartaltepe & The Poppies Team 2025) in Cycle 3 of JWST (PID 5398). Our target galaxy CGG-z7 is a compact galaxy group centered at R.A. 189.17582, Dec. 62.34485, located to the north of the GOODS-North field (M. Giavalisco et al. 2004). POPPIES (The Public Observation Pure Parallel Infrared Emission-Line Survey) is a 400-hour purely parallel survey covering $\sim 1455 \text{ arcmin}^2$. It takes grism spectra with 1–3 filters (F444W, then F322W2/F277W+F356W), as well as images in 3–8 filters over 150 fields, providing a blind emission line survey. F444W, F200W, F115W images and F444W grism spectra are available for CGG-z7. We note that CGG-z7 lies more than 0.8 arcmin away from the boundary of the conventional GOODS-North footprint, placing it outside the deep-field coverage where additional multi-band data are available. Although our target is also covered by HST/ACS and Spitzer/IRAC, these data were not included in the analysis owing to

their low signal-to-noise ratios and/or poor angular resolution.

The image reduction is based on the standard `jwst` pipeline (H. Bushouse et al. 2025) version 1.18.1 with reference file `jwst_1364.pmap`. We begin the reduction on the public uncal files from MAST⁴. We performed astrometric calibration by registering the images to *Gaia* (P. Gavras et al. 2023). The photometry catalog was then generated from the calibrated images using `photutils` (L. Bradley et al. 2025). The final mosaic images are drizzled with `pix_frac=1.0` and a pixel size of $0.03''$. The total exposure times of F444W, F200W, F115W are 1804, 8761, 1804 seconds, respectively.

The F444W grism spectra of CGG-z7 are reduced following the routine outlined by F. Sun et al. (2023); F. Sun (2024)⁵. We refer interested readers to the SAPHIRES early data release paper F. Sun et al. (2025) for further details.

3. RESULTS

3.1. Morphology

This section presents the morphology analysis of CGG-z7 based on JWST/NIRCam imaging. As shown in Fig. 1, six candidate member galaxies are clearly detected in the deep F200W exposure, four of which are spectroscopically confirmed (see Sec. 3.2). The group spans a projected area of approximately $1.5 \times 1.1 \text{ arcsec}^2$, corresponding to $\sim 7.8 \times 5.7 \text{ kpc}^2$ at its redshift. We characterize the structural properties of the member galaxies using `pysersic` (I. Pasha & T. B. Miller 2023). The analysis proceeds as follows. First, a detection map is created from the F200W image using `photutils` to identify the centroids of all group members. This map is used to generate a multi-band photometric catalog, which subsequently informs the fitting priors for `pysersic`. We then perform multi-band joint modeling, adopting a single Sérsic profile for each source in each band. During the fitting, we fix `xc,yc,theta` across the bands, and set `n,ellip,r_eff` as the linked parameters⁶. A summary of the analysis is shown in Fig. 3. The marginalized posterior of the model parameters is shown in Tab. 3. All of the members can be well fitted with a single Sérsic model. During the fitting, we use the empirical PSFs from `stpsf` (M. Perrin et al. 2025).

⁴ <https://mast.stsci.edu/portal/Mashup/Clients/Mast/Portal.html>

⁵ The codes and calibration data are available at https://github.com/fengwusun/nircam_grism/

⁶ See <https://pysersic.readthedocs.io/en/latest/multiband-example.html>

³ <https://db.chiantidatabase.org/>

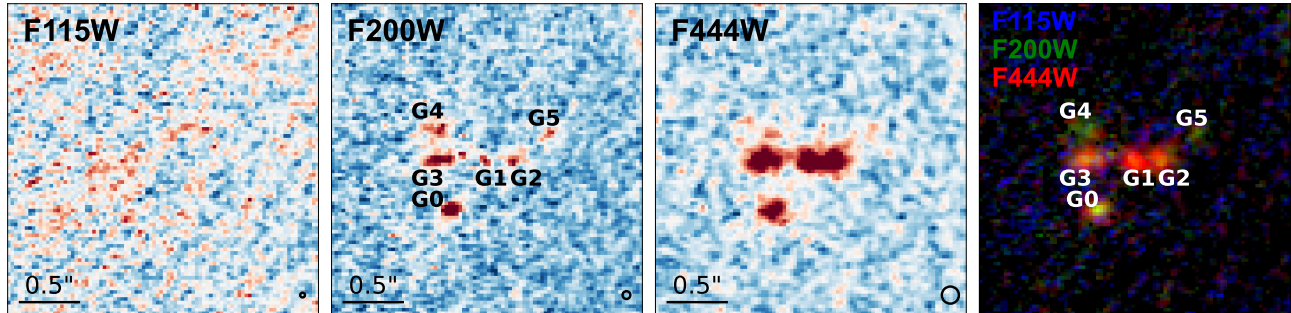


Figure 1. Multiband image of CGG-z7 (zscale). The black bar in the bottom left marks a $0.5''$ scale (2.59 kpc). The black circle in the bottom right denotes the FWHM of PSFs.

The morphological analysis yields Sérsic indices ranging from $n \sim 0.8$ to 3.4, with galaxies G0, G2, and G3 exhibiting disk or irregular profiles ($n < 2$). In the dense environment, such low- n structures are unlikely to survive multiple strong gravitational encounters if the system were old and dynamically relaxed. Thus, the n 's provide indirect evidence that CGG-z7 is a dynamically young system, consistent with the kinematic picture derived from the stellar-to-dynamical mass ratio discussed in Sec. 3.4. The diversity in Sérsic indices among the group members suggests that these galaxies may have followed different evolutionary paths prior to their assembly into the current compact configuration. Nevertheless, all members share a common characteristic of being compact ($r_{\text{eff}} \lesssim 0.8$ kpc). This combination of morphological diversity within a spatially concentrated, kinematically young system provides an interesting snapshot of early galaxy assembly, where galaxies with varied formation histories are drawn together into a single, evolving structure.

The morphology of G1 is particularly notable, as it is the most compact source in the group. Its best-fit r_{eff} s of Sérsic profile are ~ 0.056 arcsec in F444W and ~ 0.046 arcsec in F200W, while its 3σ isophotal radii (defined as $\sqrt{\text{area}/\pi}$ from the residual image after subtracting models of other members) are ~ 0.106 arcsec in F444W and ~ 0.036 arcsec in F200W. These sizes are comparable to or only slightly larger than half of the empirical PSF FWHM values (0.073 arcsec for F444W, 0.033 arcsec for F200W⁷), indicating that G1 remains largely unresolved and is likely a compact object. Its nature and implications will be further discussed in the following sections.

⁷ <https://jwst-docs.stsci.edu/jwst-near-infrared-camera/nircam-performance/nircam-point-spread-functions>

3.2. Redshift

As shown in Figure 2, galaxies G0–G3 are spectroscopically confirmed using the combination of the [O III] doublet and $H\beta$ lines, whereas G4 and G5 are too faint to be detected in the grism spectra. The spectroscopic redshift z_{spec} for each confirmed galaxy is derived by cross-correlating a line-emission template with the extracted 1D spectrum. We note that the measured redshift is a combination of the cosmological redshift z_{cos} and the Doppler redshift z_{pec} due to peculiar velocity along line-of-sight (LoS), i.e.

$$1 + z_{\text{spec},i} = (1 + z_{\text{cos},i})(1 + z_{\text{pec},i}) \quad (1)$$

$$\approx 1 + z_{\text{cos},i} + (1 + z_{\text{cos},i})v_i/c \quad (2)$$

where v_i is the peculiar velocity along the LoS. The approximation holds for $v_i \ll c$, which is valid for galaxies. Here, we assign each galaxy a single LoS velocity, neglecting internal motions such as rotation.

3.3. Kinematics of G0–G3

There's a redshift difference $\Delta z \sim 0.001$ – 0.003 among the galaxy members in CGG-z7. If it's due to z_{cos} , their distance along LoS would be greater than ~ 90 kpc, which is substantially larger than their projected distance (< 8 kpc). Such a configuration is unlikely to appear in a gravitationally bound system. Instead, our analysis favors a kinematic origin for the redshift differences. Assuming that all members of CGG-z7 share the same cosmological redshift z_{cos} recognizing that a self-gravitating galaxy group should have a net LoS velocity of zero, we estimate z_{cos} as a luminosity-weighted average of the spectroscopic redshifts:

$$\hat{z}_{\text{cos}} = \frac{\sum_i m_i z_{\text{spec},i}}{\sum_i m_i} \sim \frac{\sum_i L_i z_{\text{spec},i}}{\sum_i L_i} \quad (3)$$

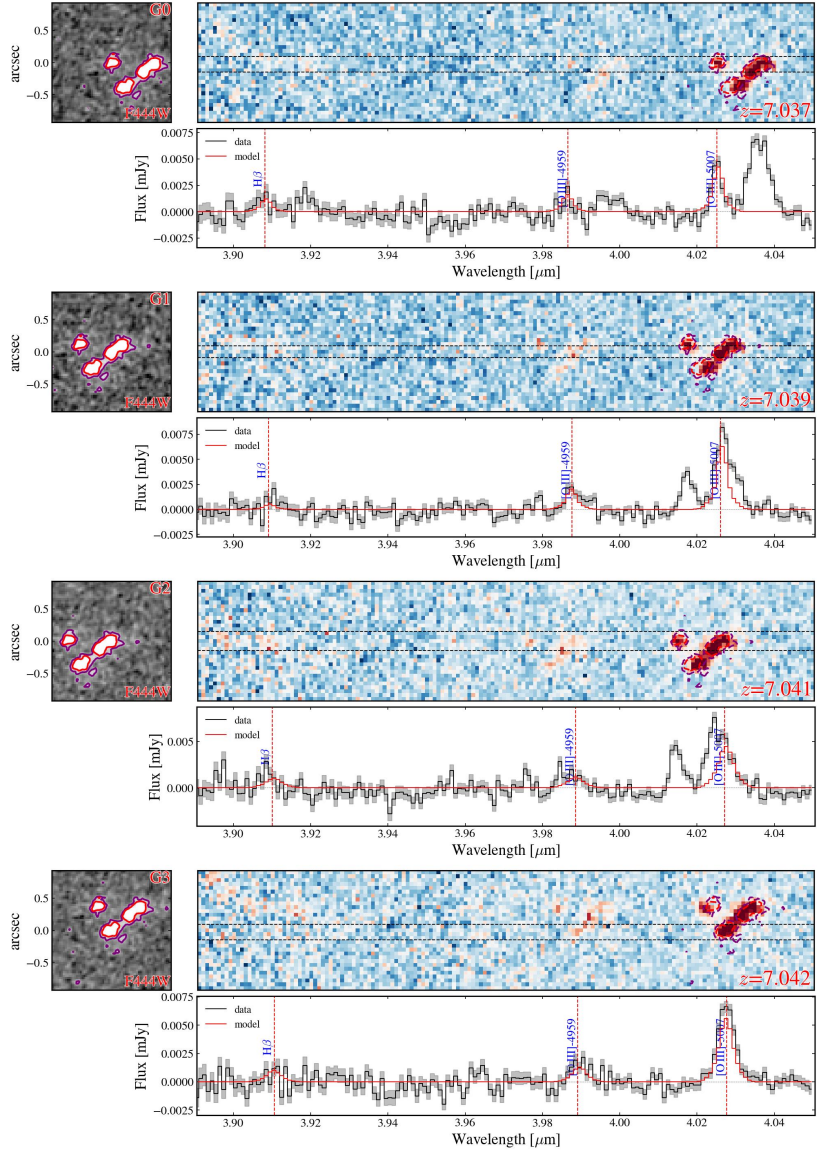


Figure 2. NIRCcam F444W grism spectra of G0–G3 obtained through Cycle 3 PID 5398 (POPPIES). The F444W images here are rotated the observed PA of 218° and flipped to match the dispersion direction of Module B of the JWST/NIRCcam. For each source, clear detections of the $H\beta$ and $[O\text{ III}]$ doublet emission lines are visible. The 3σ and 5σ source contours extracted from the direct image are overlaid onto the 2D spectra. These contours have been translated to the spectral plane using the measured spectroscopic redshift and are centered at the expected location of the $[O\text{ III}]\lambda 5007$ line.

where the summation is over G0–G3⁸, and we adopt the F444W flux as a proxy for luminosity L_i for each member. We simply assume the mass of each member is proportional to its F444W flux. Analysis gives $z_{\text{cos}} = 7.040 \pm 0.001$ for the whole group, and $v_i = -103.0, -33.7, +40.9, +78.3$ (± 35.6) km/s for G0–G3, respectively.

If we further assuming that the system is virialized, we calculate a velocity dispersion of 93.7 ± 31.7 km/s using gapper algorithm⁹ (T. C. Beers et al. 1990). Combined with the harmonic mean projected separation $R_h = 2.20$ kpc, this yields a virial mass of $M_{\text{vir}} = 3\pi\sigma_v^2 R_h / G \sim 4.2 \pm 2.7 \times 10^{10} M_\odot$ (J. Heisler et al. 1985; E. Díaz-Giménez et al. 2012; M. Tricottet et al. 2025).

⁸ This is reasonable, as G4 and G5 are significantly fainter than G0–G3, as indicated by their non-detection in the grism spectra, implying that the group’s total mass is dominated by the brighter galaxies.

⁹ Uncertainties here are estimated with the jackknife method.

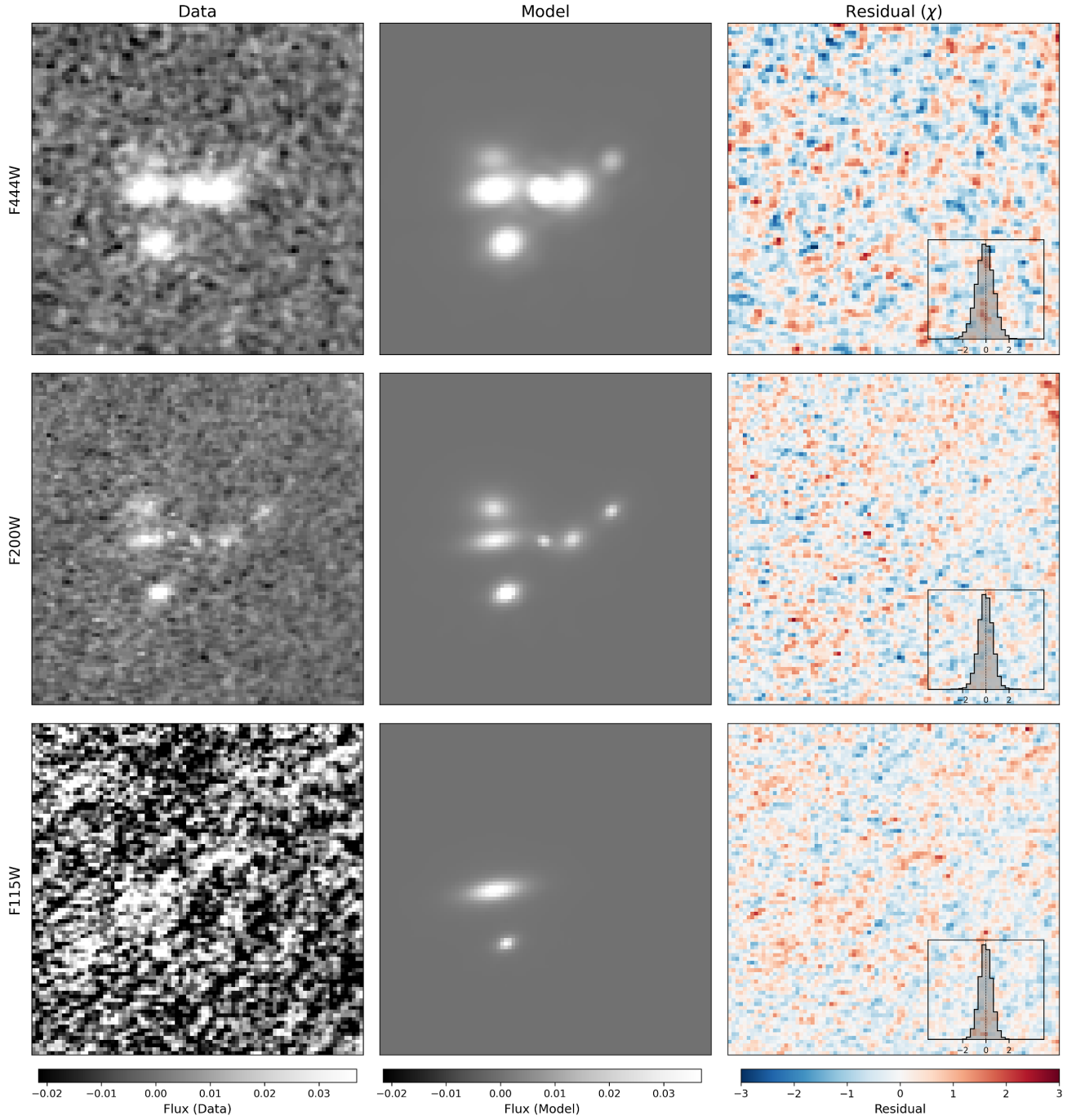


Figure 3. Multi-band morphological analysis of CGG-z7. The structure of the compact galaxy group CGG-z7 is modeled using `pysersic` with a multi-band joint fitting technique. Each row displays the results for one bandpass (F444W, F200W, and F115W, from top to bottom). Columns show, from left to right: the science image, the best-fit model, and the residual ($\chi = (\text{data} - \text{model})/\sigma_{\text{data}}$) map. The inset in each residual panel shows the normalized histogram of χ .

3.4. Stellar Masses of G0–G3

Here we derive stellar masses and other properties of the group members by performing spectral energy distribution (SED) fitting with the code `Bagpipes` (A. C. Carnall et al. 2018, 2019), which is capable of jointly fitting photometry and spectra. To ensure robustness, the analysis is restricted to galaxy G0–G3, as G4 and G5 are only marginally detected in the F444W band and thus lack sufficient signal-to-noise ratio for reliable SED constraints. Furthermore, to mitigate potential flux contamination between the closely projected members, we use the model fluxes derived from the multi-band morphological decomposition described in Sec. 3.1 rather than the raw aperture photometry. To ensure a conservative error estimate that accounts for background noise not fully captured by the fitting process alone, we adopt an error floor of 0.0033, 0.0006, and 0.0010 μJy for the F115W, F200W, and F444W bands, respectively. This floor is determined by calculating the standard deviation of fluxes measured from random apertures of 0.3 kpc radius placed on blank regions of the sky background. The joint fit incorporates the model spectra described in Sec. 3.5, serving as an additional constraint to ensure consistency across photometric and spectroscopic data.

During the fitting, we assume a delayed-tau star formation history and a Calzetti extinction law (D. Calzetti et al. 1994). The model is evaluated over the following grids: dust attenuation A_V from 0 to 2 mag, stellar population age from 1 to 500 Myr, delay timescale from 10 to 300 Myr, metallicity from 0.2 to 2 Z_\odot , ionization parameter $\log U$ from -3 to -1 . The redshift for each source is fixed to z_{cos} determined in Sec. 3.3. The results of the SED fitting, including the posterior median and credible intervals for key parameters, are summarized in Tab. 1.

The stellar masses are reasonably well constrained, with $\log(M_*/M_\odot)$ ranging from ~ 9.0 to 9.4. All galaxies show significant star formation, with SFRs between ~ 5 and 14 $M_\odot\text{yr}^{-1}$. A notable result is the uniformly low stellar metallicity $< 0.2 Z_\odot$ and a high ionization parameter $\log U > -2$ across the group, which is consistent with the extreme emission-line ratios described in Sec. 3.5. We note, however, that the SED properties of G1—including its stellar mass—may be influenced by an AGN. The posterior distributions for age remain broad and prior-sensitive. The results may suffer from degeneracies among age, dust, and star formation history in such data-sparse SED modeling. Deeper, multi-band observations with higher SNR are required to break these degeneracies and to obtain more robust constraints on the stellar populations and dust properties of these galaxies.

The SED fitting results for G0–G3 yield a total stellar mass for the group of $\log(M_*/M_\odot) = 9.80^{+0.19}_{-0.21}$. Combined with the total virial mass estimate of $\sim 4.2 \pm 2.7 \times 10^{10} M_\odot$ from Sec. 3.3, we derive a stellar-to-dynamical mass fraction of $M_*/M_{\text{vir}} \sim 0.15^{+0.20}_{-0.08}$.

This value is extraordinarily high, exceeding the typical range of 0.01 to 0.05 for galaxies and clusters¹⁰ in the local and high-redshift universe (G. Girelli et al. 2020; L. Paquereau et al. 2025). The most compelling interpretation is that the classical virial mass estimator is severely biased low because the system is not in dynamical equilibrium. The extremely high M_*/M_{vir} serves as independent, strong evidence that CGG-z7 is a dynamically young system. The low measured velocity dispersion likely reflects non-virial, possibly merging kinematics, rather than a relaxed gravitational potential. It is consistent with a scenario where the group is undergoing a major merger.

3.5. Emission-Line Properties

To obtain robust emission-line fluxes for individual member galaxies while mitigating potential contamination from their closely projected neighbours, we perform two-dimensional spectral fitting again using `pysersic`. We focus on the $\text{H}\beta$ and $[\text{O III}]\lambda\lambda 4959, 5007$ features, with cutouts of the 2D spectra for galaxies G0–G3 presented in Fig. 2. Given its highest signal-to-noise ratio (S/N), the $[\text{O III}]\lambda 5007$ line is used as a reference to define the fitting priors, including the spatial position of each galaxy’s emission. Here we set all the morphology parameters `xc`, `yc`, `theta`, `n`, `ellip`, `r_eff` of an individual galaxy to be the same for different lines, allowing only the line fluxes to vary freely.

The resulting line fluxes are summarized in Tab. 2. As a key quality check, the measured flux ratios $[\text{O III}]\lambda 4959 / [\text{O III}]\lambda 5007$ for the four galaxies are consistent with the theoretical value of 1:2.98 within 2σ (1.08σ , 0.09σ , 1.29σ , and 1.84σ for G0–G3, respectively). A comparison of data and model is shown in Fig. 5. From these fluxes, we calculate the line ratio $\text{R3} = ([\text{O III}]\lambda 4959 + [\text{O III}]\lambda 5007) / \text{H}\beta$ ¹¹, finding values in the range of approximately 5 to 18.

The elevated R3 ratios are generally indicative of extreme conditions in the ionized gas. They commonly signal a hard radiation field with high ionization parameters and/or exceptionally low gas-phase metallicity (A. Calabrò et al. 2024; J. A. Zavala et al. 2025; W.

¹⁰ We note the potential risk of overestimating M_* of G1. But even without G1, the total stellar mass of the group is $\log(M_*/M_\odot) = 9.59^{+0.19}_{-0.20}$, yielding $M_*/M_{\text{vir}} \sim 0.09^{+0.13}_{-0.05}$.

¹¹ We do not apply a dust attenuation correction here.

Table 1. SED fitting results of G0–G3 from `Bagpipes`.

Galaxy	SFR[$M_{\odot}\text{yr}^{-1}$]	$\log(M_*/M_{\odot})$	A_V	Age[Gyr]	$Z[Z_{\odot}]$	$\log U$
G0	$6.88^{+3.93}_{-2.32}$	$9.08^{+0.19}_{-0.19}$	$0.87^{+0.36}_{-0.25}$	$0.28^{+0.12}_{-0.11}$	$0.13^{+0.04}_{-0.05}$	$-1.86^{+0.55}_{-0.61}$
G1	$14.94^{+3.68}_{-4.15}$	$9.38^{+0.17}_{-0.23}$	$1.74^{+0.17}_{-0.26}$	$0.26^{+0.13}_{-0.12}$	$0.19^{+0.01}_{-0.02}$	$-1.37^{+0.27}_{-0.46}$
G2	$14.20^{+5.58}_{-4.33}$	$9.29^{+0.20}_{-0.21}$	$1.61^{+0.23}_{-0.30}$	$0.22^{+0.14}_{-0.11}$	$0.15^{+0.03}_{-0.03}$	$-1.76^{+0.53}_{-0.55}$
G3	$5.01^{+2.05}_{-1.39}$	$8.89^{+0.18}_{-0.21}$	$0.32^{+0.24}_{-0.20}$	$0.24^{+0.12}_{-0.10}$	$0.17^{+0.02}_{-0.03}$	$-1.68^{+0.50}_{-0.46}$

Table 2. Line Flux (unit: 10^{-18} erg s $^{-1}$ cm $^{-2}$). Here R3 is defined as $([\text{O III}]\lambda 4959 + [\text{O III}]\lambda 5007)/\text{H}\beta$.

Galaxy	H β	[O III] $\lambda 4959$	[O III] $\lambda 5007$	R3
G0	$0.89^{+0.20}_{-0.17}$	$1.35^{+0.21}_{-0.23}$	$3.46^{+0.26}_{-0.24}$	$5.38^{+1.49}_{-0.98}$
G1	$0.46^{+0.14}_{-0.15}$	$2.01^{+0.25}_{-0.22}$	$6.18^{+0.43}_{-0.38}$	$17.85^{+8.22}_{-4.40}$
G2	$1.11^{+0.20}_{-0.21}$	$1.36^{+0.21}_{-0.23}$	$5.29^{+0.37}_{-0.33}$	$5.98^{+1.41}_{-0.98}$
G3	$0.99^{+0.21}_{-0.19}$	$1.37^{+0.21}_{-0.20}$	$5.91^{+0.38}_{-0.26}$	$7.38^{+1.95}_{-1.35}$

McClymont et al. 2025). While R3 is commonly used as a gas-phase metallicity indicator, its application here is problematic for several reasons. Most established empirical calibrations are described with a double-branched relation with a second or third-order polynomial function peaking at $R3 \sim 8.4$ (e.g. M. Hirschmann et al. 2023; R. L. Sanders et al. 2024; P. Chakraborty et al. 2025)¹². As our R3 falls outside the valid domain or near the turnover point of these functions, and because the relation is flat near the peak, any attempt to invert it would yield degenerate solutions with large uncertainties. Moreover, such calibrations often exhibit significant intrinsic scatter, particularly at high redshifts. Low S/N of H β ($\lesssim 1.5$) and [O III] $\lambda 4959$ (~ 2) also blur the measurements. So we refrain from deriving quantitative metallicity estimates for individual galaxies in this work. The high R3 values are reported here primarily to characterize the extreme ionized gas conditions and low-metallicity within CGG-z7.

The case of G1 warrants specific attention. It exhibits the most extreme line ratio in the group ($R3 \sim 17.85$), a notably high value compared to typical star-forming galaxies (E. R. Stanway et al. 2014; M. Hirschmann et al. 2023; K. Nakajima et al. 2023; R. L. Sanders et al. 2024; P. Chakraborty et al. 2025; Z. Li et al. 2025). This, combined with its status as the most compact and barely resolved source (see Sec. 3.1) and its high ionization parameter ($\log U \sim -1.37$ from SED fitting, albeit with large uncertainty), makes G1 a compelling candidate for hosting an obscured AGN.

¹² Some of them define R3 as $[\text{O III}]\lambda 5007/\text{H}\beta$, which is 3/4 of our R3.

4. SUMMARY AND DISCUSSION

In this paper, we report the discovery of CGG-z7, a compact galaxy group at redshift ~ 7.04 , identified in public JWST/NIRCam imaging and grism data from the POPPIES program (PID 5398). The group comprises at least six member candidates detected in deep F200W imaging, four of which (G0–G3) are spectroscopically confirmed via their H β and [O III] doublet emission in the F444W grism spectra. With a projected size of only $\sim 7.8 \times 5.7$ kpc 2 , CGG-z7 is among the most compact and highest-redshift galaxy groups known to date.

4.1. Properties of CGG-z7

Multi-band morphological analysis with `pysersic` reveals that the group members have Sérsic indices in the range $n \sim 0.8 - 3.4$, all with compact sizes that $r_{\text{eff}} \lesssim 0.8$ kpc. Spectral energy distribution (SED) fitting with `Bagpipes` indicates that all G0–G3 are star-forming, metal-poor, and exhibit high ionization parameters $\log U > -2$. These properties are corroborated by strong [O III] emission, with line ratios $R3 \sim 5 - 18$ suggesting extreme ionization conditions and low gas-phase metallicity in the ionized gas.

The group’s systemic cosmological redshift is precisely measured as $z_{\text{cos}} = 7.040 \pm 0.001$. From the velocity differences of the members, we derive a line-of-sight velocity dispersion of 93.7 ± 31.7 km/s. Under the assumption of virial equilibrium, this implies a dynamical mass of $M_{\text{vir}} \approx 4.2 \pm 2.7 \times 10^{10} M_{\odot}$. However, the resulting stellar-to-dynamical mass ratio, $M_*/M_{\text{vir}} \sim 0.15^{+0.20}_{-0.08}$, is three times higher than in typical relaxed systems. This large discrepancy indicates that the classical virial mass estimator is likely biased low because CGG-z7 is not in dynamical equilibrium, pointing instead to a young, unrelaxed system that may be undergoing a merger.

4.2. G1 Hosts an AGN

In particular, the extreme properties of member G1—including its compact morphology, exceptionally high $[\text{O III}]/\text{H}\beta$ ratio and ionization parameter—strongly suggest it hosts an AGN instead of pure star formation, consistent with high-redshift AGN diagnostics in dense environments that $\log([\text{O III}]/\text{H}\beta) \gtrsim 0.8 - 1.5$ and $\log U \gtrsim -2$ (A. Calabrò et al. 2024; G. Mazzolari et al. 2025; J. Scholtz et al. 2025). This finding aligns with the established trend that galaxy interactions in compact groups substantially enhance both AGN activity and star formation, making the emergence of such an obscured AGN in CGG-z7 not uncommon (e.g. M. A. Martínez et al. 2010; D. Puskás et al. 2025; E. A. Shah et al. 2025; M. K. Shea et al. 2026). Probably fueled by frequent mergers and gas inflows, the AGN is expected to drive powerful feedback processes, suppressing future star formation and accelerating the depletion of the interstellar medium.

4.3. Fate of the Compact Galaxy Group

The properties of CGG-z7—its high star formation rate, uniformly extreme ionization state, and likely merging state—suggest it may be a direct progenitor of the massive quiescent or post-starburst galaxies observed at $z \sim 5 - 6$ (N. B. Sillassen et al. 2022; S. Jin et al. 2024; A. Saxena et al. 2025). Within the deep potential well, the intense radiation field, alongside the merger or interaction triggered starburst and AGN feedback, could rapidly consume or expel the remaining gas (A. Wilkinson et al. 2021; M. Ando et al. 2022; T. Kakimoto et al. 2024; S. Jin et al. 2024; N. B. Sillassen et al. 2024). Subsequent dynamical relaxation and quenching, possibly accelerated by the merger itself, would transform this compact group into a single, massive spheroidal quenched galaxy, i.e. a “Red Nugget”, on

a timescale of a few hundred million years (S. Jin et al. 2023; M. Brinch et al. 2025; A. Saxena et al. 2025).

CGG-z7 establishes a pivotal high-redshift benchmark; future deep, multi-wavelength integral field spectrograph (IFU) is needed to unveil its full diagnostic potential for early galaxy formation and evolution.

ACKNOWLEDGMENTS

This work is supported by Z.C. funded by National Key R&D Program of China, grantnumber 2023YFA1605600, National Natural Science Foundation of China, grantnumber 12525303, and Tsinghua University Initiative Scientific Research Program. J.W. was funded by National Natural Science Foundation of China, grant number 62222508 and 62525506. Z.C. and J.W. were funded by New Cornerstone Science Foundation through the XPLOER PRIZE.

This work is based in part on observations made with the NASA/ESA/CSA James Webb Space Telescope. The data were obtained from the Mikulski Archive for Space Telescopes at the Space Telescope Science Institute. The observations are associated with program #5398. The authors acknowledge the POPPIES team for developing their observing program with a zero-exclusive-access period.

Facilities: JWST (NIRCam)

Software: astropy (Astropy Collaboration et al. 2013, 2018, 2022), pysersic (I. Pasha & T. B. Miller 2023), photutils (L. Bradley et al. 2025), jwst (H. Bushouse et al. 2025), Bagpipes (A. C. Carnall et al. 2018, 2019), stpsf (M. Perrin et al. 2025), numpy (C. R. Harris et al. 2020), scipy (P. Virtanen et al. 2020), MyFilter (M. Li 2023).

APPENDIX

A. SUPPLEMENTARY FIGURES

Table 3 presents the full morphological fitting results for all six candidate members of CGG-z7, complementing the summary in Section 3.1. Figure 4 shows the full SED fitting results for G0–G3, and Figure 5 compares the grism spectra and the corresponding models.

REFERENCES

Ando, M., Shimasaku, K., Momose, R., et al. 2022,

MNRAS, 513, 3252, doi: [10.1093/mnras/stac1049](https://doi.org/10.1093/mnras/stac1049)

Astropy Collaboration, Robitaille, T. P., Tollerud, E. J.,

et al. 2013, A&A, 558, A33,

doi: [10.1051/0004-6361/201322068](https://doi.org/10.1051/0004-6361/201322068)

Table 3. Morphological parameters of the group members by `pysersic`.

Source	Band	Flux [nJy]	n	r_{eff} [kpc]
G0	F444W	$75.28^{+4.96}_{-4.25}$	$1.25^{+0.42}_{-0.24}$	$0.43^{+0.05}_{-0.04}$
	F200W	$35.45^{+3.18}_{-2.81}$	$1.55^{+0.60}_{-0.38}$	$0.31^{+0.04}_{-0.04}$
	F115W	$12.31^{+8.70}_{-8.27}$	$1.60^{+0.78}_{-0.47}$	$0.30^{+0.07}_{-0.07}$
G1	F444W	$83.13^{+6.12}_{-5.30}$	$2.42^{+1.35}_{-0.82}$	$0.29^{+0.05}_{-0.05}$
	F200W	$8.28^{+1.92}_{-1.95}$	$3.26^{+1.42}_{-1.20}$	$0.24^{+0.12}_{-0.09}$
	F115W	$-0.10^{+0.68}_{-0.64}$	$3.42^{+1.74}_{-1.38}$	$0.23^{+0.15}_{-0.13}$
G2	F444W	$81.07^{+5.36}_{-5.53}$	$0.97^{+0.22}_{-0.15}$	$0.47^{+0.04}_{-0.04}$
	F200W	$18.73^{+2.70}_{-3.02}$	$1.41^{+0.59}_{-0.36}$	$0.46^{+0.09}_{-0.08}$
	F115W	$-0.04^{+0.63}_{-0.66}$	$1.49^{+0.83}_{-0.43}$	$0.46^{+0.12}_{-0.12}$
G3	F444W	$97.53^{+4.87}_{-4.95}$	$0.84^{+0.13}_{-0.08}$	$0.58^{+0.04}_{-0.04}$
	F200W	$39.57^{+4.14}_{-3.71}$	$1.03^{+0.25}_{-0.14}$	$0.79^{+0.09}_{-0.08}$
	F115W	$57.78^{+14.78}_{-15.38}$	$1.05^{+0.31}_{-0.18}$	$0.90^{+0.12}_{-0.13}$
G4	F444W	$33.72^{+5.60}_{-5.41}$	$1.07^{+0.41}_{-0.22}$	$0.78^{+0.13}_{-0.13}$
	F200W	$37.29^{+5.40}_{-4.81}$	$1.38^{+0.42}_{-0.29}$	$0.77^{+0.11}_{-0.12}$
	F115W	$-0.03^{+0.67}_{-0.64}$	$1.45^{+0.58}_{-0.37}$	$0.77^{+0.14}_{-0.15}$
G5	F444W	$14.58^{+3.59}_{-2.87}$	$3.16^{+2.11}_{-1.44}$	$0.22^{+0.15}_{-0.15}$
	F200W	$12.24^{+2.61}_{-2.54}$	$3.12^{+1.87}_{-1.25}$	$0.36^{+0.11}_{-0.10}$
	F115W	$-0.05^{+0.69}_{-0.69}$	$3.14^{+1.90}_{-1.34}$	$0.39^{+0.14}_{-0.12}$

- Astropy Collaboration, Price-Whelan, A. M., Sipőcz, B. M., et al. 2018, *AJ*, 156, 123, doi: [10.3847/1538-3881/aabc4f](https://doi.org/10.3847/1538-3881/aabc4f)
- Astropy Collaboration, Price-Whelan, A. M., Lim, P. L., et al. 2022, *ApJ*, 935, 167, doi: [10.3847/1538-4357/ac7c74](https://doi.org/10.3847/1538-4357/ac7c74)
- Beers, T. C., Flynn, K., & Gebhardt, K. 1990, *AJ*, 100, 32, doi: [10.1086/115487](https://doi.org/10.1086/115487)
- Bradley, L., Sipőcz, B., Robitaille, T., et al. 2025, *astropy/photutils: 2.2.0*, 2.2.0 Zenodo, doi: [10.5281/zenodo.14889440](https://doi.org/10.5281/zenodo.14889440)
- Brinch, M., Jin, S., Gobat, R., et al. 2025, *A&A*, 694, A218, doi: [10.1051/0004-6361/202451448](https://doi.org/10.1051/0004-6361/202451448)
- Bushouse, H., Eisenhamer, J., Dencheva, N., et al. 2025, *JWST Calibration Pipeline*, Zenodo (CERN European Organization for Nuclear Research) doi: [10.5281/zenodo.15632984](https://doi.org/10.5281/zenodo.15632984)
- Calabrò, A., Castellano, M., Zavala, J. A., et al. 2024, *ApJ*, 975, 245, doi: [10.3847/1538-4357/ad7602](https://doi.org/10.3847/1538-4357/ad7602)
- Calzetti, D., Kinney, A. L., & Storchi-Bergmann, T. 1994, *ApJ*, 429, 582, doi: [10.1086/174346](https://doi.org/10.1086/174346)
- Carnall, A. C., McLure, R. J., Dunlop, J. S., & Davé, R. 2018, *MNRAS*, 480, 4379, doi: [10.1093/mnras/sty2169](https://doi.org/10.1093/mnras/sty2169)
- Carnall, A. C., McLure, R. J., Dunlop, J. S., et al. 2019, *MNRAS*, 490, 417, doi: [10.1093/mnras/stz2544](https://doi.org/10.1093/mnras/stz2544)
- Carnall, A. C., McLure, R. J., Dunlop, J. S., et al. 2023, *Nature*, 619, 716, doi: [10.1038/s41586-023-06158-6](https://doi.org/10.1038/s41586-023-06158-6)
- Chakraborty, P., Sarkar, A., Smith, R., et al. 2025, *ApJ*, 985, 24, doi: [10.3847/1538-4357/adc7b5](https://doi.org/10.3847/1538-4357/adc7b5)
- Chiang, Y.-K., Overzier, R., & Gebhardt, K. 2013, *ApJ*, 779, 127, doi: [10.1088/0004-637X/779/2/127](https://doi.org/10.1088/0004-637X/779/2/127)
- Chiang, Y.-K., Overzier, R. A., Gebhardt, K., & Henriques, B. 2017, *ApJL*, 844, L23, doi: [10.3847/2041-8213/aa7e7b](https://doi.org/10.3847/2041-8213/aa7e7b)
- Comerford, J. M., & Greene, J. E. 2014, *ApJ*, 789, 112, doi: [10.1088/0004-637X/789/2/112](https://doi.org/10.1088/0004-637X/789/2/112)
- de Graaff, A., Setton, D. J., Brammer, G., et al. 2025, *Nature Astronomy*, 9, 280, doi: [10.1038/s41550-024-02424-3](https://doi.org/10.1038/s41550-024-02424-3)
- Dekel, A., & Burkert, A. 2014, *MNRAS*, 438, 1870, doi: [10.1093/mnras/stt2331](https://doi.org/10.1093/mnras/stt2331)
- Del Zanna, G., Dere, K. P., Young, P. R., & Landi, E. 2021, *ApJ*, 909, 38, doi: [10.3847/1538-4357/abd8ce](https://doi.org/10.3847/1538-4357/abd8ce)
- Dere, K. P., Landi, E., Mason, H. E., Monsignori Fossi, B. C., & Young, P. R. 1997, *A&AS*, 125, 149, doi: [10.1051/aas:1997368](https://doi.org/10.1051/aas:1997368)
- Díaz-Giménez, E., Mamon, G. A., Pacheco, M., Mendes de Oliveira, C., & Alonso, M. V. 2012, *MNRAS*, 426, 296, doi: [10.1111/j.1365-2966.2012.21705.x](https://doi.org/10.1111/j.1365-2966.2012.21705.x)
- Díaz-Santos, T., Assef, R. J., Blain, A. W., et al. 2018, *Science*, 362, 1034, doi: [10.1126/science.aap7605](https://doi.org/10.1126/science.aap7605)
- Fudamoto, Y., Nakazato, Y., Ceverino, D., et al. 2025, *arXiv e-prints*, arXiv:2510.11770, doi: [10.48550/arXiv.2510.11770](https://doi.org/10.48550/arXiv.2510.11770)

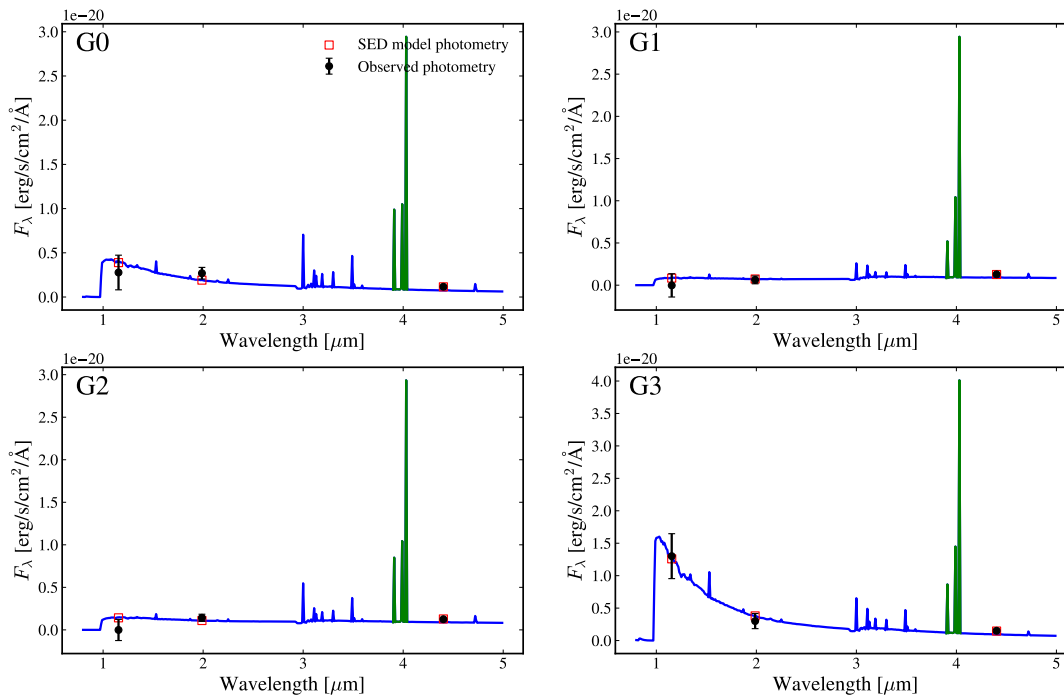


Figure 4. SEDs of G0–G3 in CGG-z7. The observed photometry means the model fluxes derived by `pysersic`. The best-fit models (blue lines) are obtained by jointly fitting the photometry and the F444W grism spectra; the segments highlighted in green indicate the wavelength ranges constrained by the grism data.

- Gavras, P., Rimoldini, L., Nienartowicz, K., et al. 2023, *A&A*, 674, A22, doi: [10.1051/0004-6361/202244367](https://doi.org/10.1051/0004-6361/202244367)
- Giavalisco, M., Ferguson, H. C., Koekemoer, A. M., et al. 2004, *ApJL*, 600, L93, doi: [10.1086/379232](https://doi.org/10.1086/379232)
- Girelli, G., Bolzonella, M., & Cimatti, A. 2019, *A&A*, 632, A80, doi: [10.1051/0004-6361/201834547](https://doi.org/10.1051/0004-6361/201834547)
- Girelli, G., Pozzetti, L., Bolzonella, M., et al. 2020, *A&A*, 634, A135, doi: [10.1051/0004-6361/201936329](https://doi.org/10.1051/0004-6361/201936329)
- Harris, C. R., Millman, K. J., van der Walt, S. J., et al. 2020, *Nature*, 585, 357, doi: [10.1038/s41586-020-2649-2](https://doi.org/10.1038/s41586-020-2649-2)
- Heisler, J., Tremaine, S., & Bahcall, J. N. 1985, *ApJ*, 298, 8, doi: [10.1086/163584](https://doi.org/10.1086/163584)
- Hickson, P. 1997, *ARA&A*, 35, 357, doi: [10.1146/annurev.astro.35.1.357](https://doi.org/10.1146/annurev.astro.35.1.357)
- Hirschmann, M., Charlot, S., & Somerville, R. S. 2023, *MNRAS*, 526, 3504, doi: [10.1093/mnras/stad2745](https://doi.org/10.1093/mnras/stad2745)
- Hopkins, P. F., & Quataert, E. 2011, *MNRAS*, 415, 1027, doi: [10.1111/j.1365-2966.2011.18542.x](https://doi.org/10.1111/j.1365-2966.2011.18542.x)
- Jin, S., Sillassen, N. B., Magdis, G. E., et al. 2023, *A&A*, 670, L11, doi: [10.1051/0004-6361/202245724](https://doi.org/10.1051/0004-6361/202245724)
- Jin, S., Sillassen, N. B., Magdis, G. E., et al. 2024, *A&A*, 683, L4, doi: [10.1051/0004-6361/202348540](https://doi.org/10.1051/0004-6361/202348540)
- Kakimoto, T., Tanaka, M., Onodera, M., et al. 2024, *ApJ*, 963, 49, doi: [10.3847/1538-4357/ad1ff1](https://doi.org/10.3847/1538-4357/ad1ff1)
- Kartalpe, J., & The Poppies Team. 2025, in *American Astronomical Society Meeting Abstracts*, Vol. 246, 246th Meeting of the American Astronomical Society, 209.09
- Lapiner, S., Dekel, A., Freundlich, J., et al. 2023, *MNRAS*, 522, 4515, doi: [10.1093/mnras/stad1263](https://doi.org/10.1093/mnras/stad1263)
- Li, M. 2023, *MyFilter: A Web Application for Interactive Visualization of Astronomical Filter Transmission Curves*, 1.0.0 Zenodo, doi: [10.5281/zenodo.10210202](https://doi.org/10.5281/zenodo.10210202)
- Li, M., Emonts, B. H. C., Cai, Z., et al. 2026, *ApJ*, 999, 40, doi: [10.3847/1538-4357/ae3c10](https://doi.org/10.3847/1538-4357/ae3c10)
- Li, Z., Cai, Z., Wang, X., et al. 2025, *ApJS*, 280, 62, doi: [10.3847/1538-4365/adfa70](https://doi.org/10.3847/1538-4365/adfa70)
- Liu, S., Zheng, X. Z., Gonzalez, V., et al. 2025, *MNRAS*, 536, 2000, doi: [10.1093/mnras/stae2746](https://doi.org/10.1093/mnras/stae2746)
- Martínez, M. A., Del Olmo, A., Coziol, R., & Perea, J. 2010, *AJ*, 139, 1199, doi: [10.1088/0004-6256/139/3/1199](https://doi.org/10.1088/0004-6256/139/3/1199)
- Mazzolari, G., Scholtz, J., Maiolino, R., et al. 2025, *A&A*, 700, A12, doi: [10.1051/0004-6361/202451860](https://doi.org/10.1051/0004-6361/202451860)
- McClymont, W., Smith, A., & Tacchella, S. 2025, *arXiv e-prints*, arXiv:2510.13952, doi: [10.48550/arXiv.2510.13952](https://doi.org/10.48550/arXiv.2510.13952)

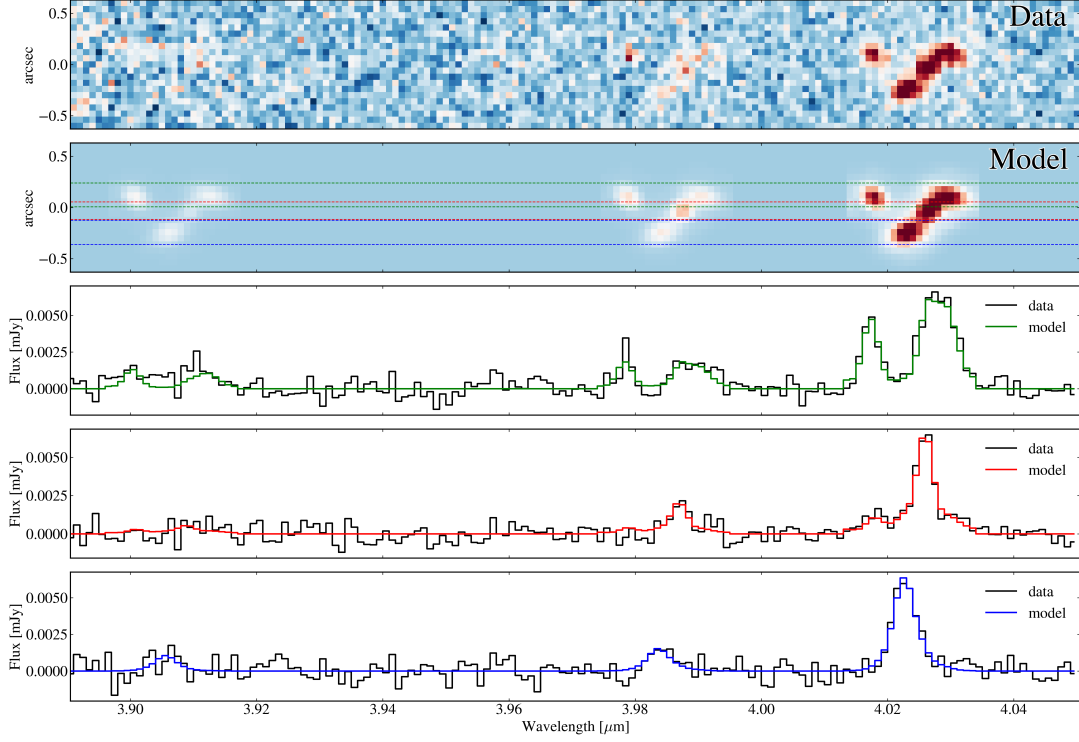


Figure 5. F444W grism spectra (black) and the corresponding model spectra from `pysersic` (colored lines). The green, red, and blue lines show the 1D model spectra for the regions between the pairs of horizontal dashed lines of the same color.

- Nakajima, K., Ouchi, M., Isobe, Y., et al. 2023, *ApJS*, 269, 33, doi: [10.3847/1538-4365/acd556](https://doi.org/10.3847/1538-4365/acd556)
- Paquereau, L., Laigle, C., McCracken, H. J., et al. 2025, *A&A*, 702, A163, doi: [10.1051/0004-6361/202553828](https://doi.org/10.1051/0004-6361/202553828)
- Pasha, I., & Miller, T. B. 2023, *The Journal of Open Source Software*, 8, 5703, doi: [10.21105/joss.05703](https://doi.org/10.21105/joss.05703)
- Perrin, M., Long, J., Osborne, S., et al. 2025, *STPSF* (2.1.0), Zenodo doi: [10.5281/zenodo.15747364](https://doi.org/10.5281/zenodo.15747364)
- Puskás, D., Tacchella, S., Simmonds, C., et al. 2025, arXiv e-prints, arXiv:2510.14743, doi: [10.48550/arXiv.2510.14743](https://doi.org/10.48550/arXiv.2510.14743)
- Sanders, R. L., Shapley, A. E., Topping, M. W., Reddy, N. A., & Brammer, G. B. 2024, *ApJ*, 962, 24, doi: [10.3847/1538-4357/ad15fc](https://doi.org/10.3847/1538-4357/ad15fc)
- Saxena, A., Overzier, R. A., Aydar, C., et al. 2025, arXiv e-prints, arXiv:2511.13650, doi: [10.48550/arXiv.2511.13650](https://doi.org/10.48550/arXiv.2511.13650)
- Scholtz, J., Maiolino, R., D'Eugenio, F., et al. 2025, *A&A*, 697, A175, doi: [10.1051/0004-6361/202348804](https://doi.org/10.1051/0004-6361/202348804)
- Shah, E. A., Lemaux, B. C., Forrest, B., et al. 2025, *A&A*, 704, A101, doi: [10.1051/0004-6361/202452055](https://doi.org/10.1051/0004-6361/202452055)
- Shea, M. K., Crenshaw, D. M., Fischer, T. C., et al. 2026, *ApJ*, 997, 208, doi: [10.3847/1538-4357/ae2796](https://doi.org/10.3847/1538-4357/ae2796)
- Sillassen, N. B., Jin, S., Magdis, G. E., et al. 2022, *A&A*, 665, L7, doi: [10.1051/0004-6361/202244661](https://doi.org/10.1051/0004-6361/202244661)
- Sillassen, N. B., Jin, S., Magdis, G. E., et al. 2024, *A&A*, 690, A55, doi: [10.1051/0004-6361/202450760](https://doi.org/10.1051/0004-6361/202450760)
- Somerville, R. S., & Davé, R. 2015, *ARA&A*, 53, 51, doi: [10.1146/annurev-astro-082812-140951](https://doi.org/10.1146/annurev-astro-082812-140951)
- Staab, P., Lemaux, B. C., Forrest, B., et al. 2024, *MNRAS*, 528, 6934, doi: [10.1093/mnras/stae301](https://doi.org/10.1093/mnras/stae301)
- Stanway, E. R., Eldridge, J. J., Greis, S. M. L., et al. 2014, *MNRAS*, 444, 3466, doi: [10.1093/mnras/stu1682](https://doi.org/10.1093/mnras/stu1682)
- Sun, F. 2024, *nircam_grism*, 3.0 Zenodo, doi: [10.5281/zenodo.14052875](https://doi.org/10.5281/zenodo.14052875)
- Sun, F., Egami, E., Pirzkal, N., et al. 2023, *ApJ*, 953, 53, doi: [10.3847/1538-4357/acd53c](https://doi.org/10.3847/1538-4357/acd53c)
- Sun, F., Fudamoto, Y., Lin, X., et al. 2025, arXiv e-prints, arXiv:2503.15587, doi: [10.48550/arXiv.2503.15587](https://doi.org/10.48550/arXiv.2503.15587)
- Tacchella, S., Dekel, A., Carollo, C. M., et al. 2016, *MNRAS*, 457, 2790, doi: [10.1093/mnras/stw131](https://doi.org/10.1093/mnras/stw131)
- Tricottet, M., Mamon, G. A., & Díaz-Giménez, E. 2025, *A&A*, 699, A329, doi: [10.1051/0004-6361/202451713](https://doi.org/10.1051/0004-6361/202451713)
- Virtanen, P., Gommers, R., Oliphant, T. E., et al. 2020, *Nature Methods*, 17, 261, doi: [10.1038/s41592-019-0686-2](https://doi.org/10.1038/s41592-019-0686-2)
- Wilkinson, A., Almaini, O., Wild, V., et al. 2021, *MNRAS*, 504, 4533, doi: [10.1093/mnras/stab965](https://doi.org/10.1093/mnras/stab965)
- Witten, C., Oesch, P. A., McClymont, W., et al. 2025, arXiv e-prints, arXiv:2507.06284, doi: [10.48550/arXiv.2507.06284](https://doi.org/10.48550/arXiv.2507.06284)

- Zavala, J. A., Castellano, M., Akins, H. B., et al. 2025,
Nature Astronomy, 9, 155,
doi: [10.1038/s41550-024-02397-3](https://doi.org/10.1038/s41550-024-02397-3)
- Zhou, L., Wang, T., Daddi, E., et al. 2024, A&A, 684,
A196, doi: [10.1051/0004-6361/202348351](https://doi.org/10.1051/0004-6361/202348351)